

Geothermal resource exploration by using Numerical simulation and comprehensive geophysical method

Yang Yang (✉ sxwcyyy@163.com)

Guilin University of Technology <https://orcid.org/0000-0001-5272-5060>

Bin Xiong

Guilin University of Technology

Sanxi Peng

Guilin University of Technology

Ibrar Iqbal

Guilin University of Technology

Tianyu Zhang

Guilin University of Technology

Research Article

Keywords: Geothermal Exploration, Numerical simulation, CSAMT, TEM, Geophysical exploration

Posted Date: August 26th, 2021

DOI: <https://doi.org/10.21203/rs.3.rs-828808/v1>

License:   This work is licensed under a Creative Commons Attribution 4.0 International License.

[Read Full License](#)

1 Geothermal resource exploration by using Numerical simulation and 2 comprehensive geophysical method

3
4 Yang Yang, Bin Xiong*, Sanxi Peng, Ibrar Iqbal**, Tianyu Zhang

5 College of Geosciences, Guilin University of Technology, Guilin, Guangxi, China.

6 Corresponding author: Bin Xiong, xiongbn@msn.com; Ibrar Iqbal, ibrariqbal@glut.edu.cn;

7 8 **Abstract :**

9 Geothermal energy is an important renewable clean energy resource with high development and usage potential.
10 Geothermal resources, on the other hand, are buried deep below, and mining hazards are significant. Geophysical
11 investigation is frequently required to determine the depth and location of geothermal resources. The Transient
12 Electromagnetic Method (TEM) and the Controlled Source Audio Frequency Magnetotellurics (CSAMT) have the
13 highest detection efficiency and accuracy of all electromagnetic exploration methods. This article initially explains
14 the algorithm theory of the finite difference technique before establishing a simplified geothermal system resistivity
15 model. Established on the simplified resistivity model, a simulation analysis of the ability of CSAMT and TEM to
16 distinguish target body faults at different resistivities and dip angles was performed, and the effectiveness and
17 difference of the two methods in detecting typical geothermal resource targets was verified. A complete exploratory
18 research of CSAMT and TEM was conducted in Huaiaren County, Shuozhou City, Shanxi Province, China, based on
19 theoretical analysis. Both approaches can reflect the geoelectric structure of the survey region, demonstrating the
20 efficacy of the two methods in detecting genuine geothermal resources.

21 **Key words:** Geothermal Exploration, Numerical simulation, CSAMT, TEM, Geophysical exploration.

22 **Introduction**

23 As a green, low-carbon clean energy, geothermal resources have huge reserves and are widely distributed in
24 China. However, currently utilized geothermal resources in China are less than 5% of the reserves, and further
25 development and utilization of geothermal resources have broad prospects (Shi B, 2005). The buried depth of
26 geothermal resources is generally large, most of which have exceeded 2000m, and the risks taken during mining are
27 great. In order to have a clearer understanding and understanding of geothermal resources, it is necessary to conduct
28 a geological survey of geothermal resources before mining to find out the depth, location and reserves of geothermal
29 resources. In the exploration of geothermal resources, geophysical methods are an effective method (Wang G et al.,
30 2000; Yang L, 2017; Kang F, 2018).

31 Among the geophysical methods, Controlled Source Audio-frequency Magnetotellurics (CSAMT), Transient
32 Electromagnetic Method (TEM) are relatively effective methods for the exploration of geothermal resources, but
33 each method has its own limitations (Muraoka H et al., 1998; Spitzer K, 1995; Yang Y et al., 2009; Wang L et al.,
34 2018; Iqbal I et al., 2021). In recent years, comprehensive geophysical exploration methods (mainly CSAMT,
35 supplemented by TEM) have been used to explore geothermal resources, and achieved good results (Munoz Gerard,
36 2004; Yin M et al., 2007; Di Q et al., 2008; Zhao X et al., 2015).

37 However, most of the past geothermal resource exploration focused on engineering applications, and there were
38 few geophysical numerical simulation studies, that is why in this paper we focused to correlate the numerical
39 simulation with geophysical field data applicability. The ability of taking topography into account in a forward solver
40 greatly depends on the numerical method. The finite difference approach used to be a popular method in the past but
41 it is restricted only to be used in areas with flat topography (Spitzer K, 1995; Mufti IR, 1976). Alternatively, the
42 integral equation method is usually valid for simple structures (Dieter K et al., 1969; Okabe M, 1981). Including
43 complex topography and substructures in the modelling remains difficult with such methods. The finite element

44 approach was first introduced in the resistivity problem by Coggon (1971) and later further developed by many other
45 authors. It appears to be a flexible method to model both topography and possibly complicated geometries. Initially,
46 finite element modelling codes including topography were defined on distorted grids, using quadrangular or
47 hexahedral elements, and were thus limited to undulating topography. These approaches using block-oriented
48 meshes are also limited regarding the possibility of effective mesh refinements. Only recently, codes have been
49 developed on unstructured tetrahedral meshes; allowing for complex geometries and local mesh refinements,
50 especially around source locations. In parallel, surface integral methods are also available, with the advantage of only
51 discretizing the top interface

52 Independent of the numerical scheme, a resistivity forward solver consists of solving the electrical boundary
53 value problem for every source location. The solution of such a system of linear equations shows a singularity at the
54 source location. This leads to significant numerical errors in the vicinity of the electrode position. The singularity
55 removal technique introduced to splits the potential into a singular part, related to the source, and a residual part
56 taking into account a possible non-homogeneous conductivity model. The singular part is defined analytically for flat
57 topography. For non-flat topography, the singular component is usually computed numerically. Even with local mesh
58 refinement around the sources, a highly accurate solution is however difficult to be obtained as the objective is to
59 estimate a singular function (Günther T et al., 2006). With a thorough description and history of TEM and its
60 modeling, we discovered that TEM has never been utilized for geothermal research, and if it has been used, it has
61 never been coupled with numerical simulation. This research will demonstrate the relationship and significance of
62 numerical simulation and physical investigation in their respective fields of study. Furthermore, it is not required in
63 any investigation that numerical simulation produce equally exact and matched results with field data, but it does
64 provide a hint for future exploration in the field that is the subject of this study. We primarily simulate and evaluate
65 the anomalies induced by changes in the resistivity, inclination, and width of the low-blocking layer in the simplified
66 model of the geothermal system's resistivity using CSAMT and TEM. Evaluate the anomalies induced by changes in

67 the resistivity, inclination, and width of the low-blocking layer in the simplified model of the geothermal system's
 68 resistivity using CSAMT and TEM (Spichak et al., 2009).

69 **Numerical simulation of electromagnetic method based on finite difference**

70 The finite difference time domain (FDTD) method is applied in the numerical simulation. The finite difference
 71 time domain technique solves Maxwell equations directly in the time domain, bypassing the procedure of first
 72 calculating the frequency domain answer and then getting the time domain response using the inverse Fourier
 73 transform. The Maxwell equations in uniform, unconsolidated and passive media can be expressed as:

$$\begin{aligned}
 \nabla \times \mathbf{E} &= -\frac{\partial \mathbf{B}(\mathbf{r}, t)}{\partial t}, \\
 \nabla \times \mathbf{H}(\mathbf{r}, t) &= \varepsilon \frac{\partial \mathbf{E}}{\partial t} + \sigma \mathbf{E}, \\
 \nabla \cdot \mathbf{E}(\mathbf{r}, t) &= 0, \\
 \nabla \cdot \mathbf{H}(\mathbf{r}, t) &= 0.
 \end{aligned}
 \tag{1}$$

75 Whereas, E is the electric field intensity, H is the magnetic field intensity, B is the magnetic flux density, σ is the
 76 electrical conductivity, ε is the dielectric constant, and t is the time. Taking the curl of Faraday's law of
 77 electromagnetic induction in equation (1), and considering Coulomb's law, the homogeneous damped wave
 78 equations of electric and magnetic fields can be obtained:

$$\nabla^2 \mathbf{E} - \mu \varepsilon \frac{\partial^2 \mathbf{E}}{\partial t^2} - \mu \sigma \frac{\partial \mathbf{E}}{\partial t} = 0.
 \tag{2}$$

80 After disregarding the displacement current, Maxwell's equations (2) in the active medium must contain the
 81 source current term, which is amended as follows;

$$\nabla \times \mathbf{H}(\mathbf{r}, t) = \varepsilon \frac{\partial \mathbf{E}}{\partial t} + \sigma \mathbf{E} + \mathbf{J}_s
 \tag{3}$$

83 Where, \mathbf{J}_s represents the source current density. At this time, according to the Yee unit cell format and the
 84 coordinate system discrete grid, the equation (3) can be spatially discrete. At the same time, since only electric or
 85 magnetic fields are sampled at the same time, on the time axis, electric and magnetic fields are sampled alternately.

86 Therefore, a uniform time grid is sampled, and the sampling interval is half a time step. When the grid form and time
 87 sampling method are adopted, equation (3) can be expressed as:

$$88 \quad \begin{cases} \frac{\partial H_z}{\partial y} - \frac{\partial H_y}{\partial z} = \gamma \frac{\partial E_x}{\partial t} + \sigma E_x + \begin{cases} J_{sx} \\ 0 \end{cases} \\ \frac{\partial H_x}{\partial z} - \frac{\partial H_z}{\partial x} = \gamma \frac{\partial E_y}{\partial t} + \sigma E_y + \begin{cases} 0 \\ J_{sy} \end{cases} \\ \frac{\partial H_y}{\partial x} - \frac{\partial H_x}{\partial y} = \gamma \frac{\partial E_z}{\partial t} + \sigma E_z \end{cases} \quad (4)$$

89 Since the excitation source current is in the xoy plane, there is no z-direction component of the source current,
 90 and only Jsx and Jsy components exist in the equation.

91 Furthermore, the difference scheme of the electric field FDTD iteration in the active medium.

$$92 \quad E_x^{n+1}(i+1/2, j, k) = \frac{2\gamma - \sigma(i+1/2, j, k)\Delta t}{2\gamma + \sigma(i+1/2, j, k)\Delta t} \cdot E_x^n(i+1/2, j, k) \\ \left[\frac{H_z^{n+1/2}(i+1/2, j+1/2, k) - H_z^{n+1/2}(i+1/2, j-1/2, k)}{\Delta y} \right. \\ \left. - \frac{H_y^{n+1/2}(i+1/2, j, k+1/2) - H_y^{n+1/2}(i+1/2, j, k-1/2)}{\Delta z} \right] \\ - \frac{2\Delta t}{2\gamma + \sigma(i+1/2, j, k)\Delta t} J_{sx}^{n+1/2}, \quad (5)$$

$$93 \quad E_y^{n+1}(i, j+1/2, k) = \frac{2\gamma - \sigma(i, j+1/2, k)\Delta t}{2\gamma + \sigma(i, j+1/2, k)\Delta t} \cdot E_y^n(i, j+1/2, k) \\ \left[\frac{H_x^{n+1/2}(i, j+1/2, k+1/2) - H_x^{n+1/2}(i, j+1/2, k-1/2)}{\Delta z} \right. \\ \left. - \frac{H_z^{n+1/2}(i+1/2, j+1/2, k) - H_z^{n+1/2}(i-1/2, j+1/2, k)}{\Delta x} \right] \\ - \frac{2\Delta t}{2\gamma + \sigma(i, j+1/2, k)\Delta t} J_{sy}^{n+1/2}, \quad (6)$$

94 The excitation source loading mode is only related to the x or y component of the electric field, so the iterative
 95 formula of Ez is the same as that of the passive region.

96 The radiation conditions are the regional boundary conditions, and the converging boundary conditions are the
 97 ground-air boundary and the stratum and anomalous body boundary. The connection criteria between the formation

98 and the aberrant body are automatically met in the Yee grid cell computation of FDTD, and no extra treatment is
 99 required. Therefore, the ground-air boundary conditions are mainly considered here.

100 The truncated boundary of the underground space is easier to meet the conditions of the far field, but it is not
 101 easy to meet the air area. In addition, there is a large difference between the aerial grid step length and the
 102 underground grid step length. According to the principle of canceling the scale, a considerable part of the calculation
 103 will be used in the non-key investigation area of the ground M-TEM. Therefore, a special solution is required.

104 In the quasi-steady state of the geophysical time-varying field, the air field satisfies the Laplace equation as:

$$105 \quad \nabla^2 \mathbf{B} = \mu_0 \nabla^2 \mathbf{H} = 0 \quad (7)$$

106 Based on this, the wave number domain equation can be derived as:

$$107 \quad B'_x(u, v, z = 0) = -\frac{iu}{\sqrt{u^2+v^2}} B'_z(u, v, z = 0) \quad (8a)$$

$$108 \quad B'_y(u, v, z = 0) = -\frac{iv}{\sqrt{u^2+v^2}} B'_z(u, v, z = 0) \quad (8b)$$

109
 110 In the formula, B'_x and B'_y are the Fourier transform of B_x and B_y , respectively, u and v are variables in
 111 the wavenumber domain, corresponding to x and y respectively.

112 3D uses the 2D Fourier transform used to process the ground-air boundary as follows

$$113 \quad F(u, v) = \int_{-x}^x \int_{-y}^y f(x, y) \exp[-i(ux + vy)] dx dy \quad (9)$$

114 From this, the, in formula (8) B'_x and B'_y can be extended upward to a grid in the air, namely

$$115 \quad B'_x(u, v, z = -h) = \exp(-h\sqrt{u^2 + v^2}) B'_x(u, v, z = 0) \quad (10)$$

$$116 \quad B'_y(u, v, z = -h) = \exp(-h\sqrt{u^2 + v^2}) B'_y(u, v, z = 0) \quad (11)$$

117 Substituting formula (8) into the above formula, we get

$$118 \quad B'_x(u, v, z = -h) = -\frac{iu}{\sqrt{u^2+v^2}} \exp(-h\sqrt{u^2 + v^2}) B'_z(u, v, z = 0) \quad (12)$$

$$119 \quad B'_y(u, v, z = -h) = -\frac{iv}{\sqrt{u^2+v^2}} \exp(-h\sqrt{u^2 + v^2}) B'_z(u, v, z = 0) \quad (13)$$

120 The Fourier transform on the ground-air boundary uses the fast Fourier algorithm. In order to meet the
121 requirements of discrete Fourier uniform grids, different processing methods are adopted according to the
122 characteristics of grid division

123 1) Non-uniform grid. The uniform grid is interpolated by nonlinear interpolation algorithms such as cubic spline
124 and five-point cubic smoothing, and after fast Fourier transform and inverse transformation continuation, the
125 interpolation method is used to restore the original grid again.

126 2) Non-uniform grid. If the nonlinear interpolation has excessive fluctuations that affect the calculation accuracy,
127 you can change to the linear interpolation trial calculation.

128 3) Uniform grid. Fourier transform and inverse transform can be directly performed without interpolation, and a
129 grid that is more suitable for discrete Fourier transform can be obtained by linear interpolation according to $2n$
130 interpolation.

131 In brief, when there is an issue with simulation accuracy, grid interpolation of the discrete Fourier transform, as
132 a component of simulation software, can be used to enhance accuracy and identify a factor that influences accuracy.
133 Through the iterative solution and the relationship between the electric field and the magnetic field, the response of
134 the electromagnetic field at each time can be obtained.

135 **NUMERICAL MODELING**

136 According to the relative relation of the resistivity of the basic elements of the geothermal system, a simplified
137 resistivity model of the geothermal system is designed for the common faults in the geothermal system that show low
138 resistance due to water conduction.

139 The numerical simulation program is the open source code SIMPEG for writing papers on the Geophysical
140 Tablet of the University of British Columbia, and the method is the finite difference method.

141 Considering the high resistance properties of deep intrusive igneous rocks that may occur, the resistivity of the
142 basement in the model is set to high resistance. The basic model consists of four-layer models with shallow and deep
143 resistivities of $100\Omega\cdot\text{m}$, $200\Omega\cdot\text{m}$, $500\Omega\cdot\text{m}$ and $1000\Omega\cdot\text{m}$, as shown in the Fig. 1(a). Considering that faults will
144 cause strata dislocation, on the basis of the basic model in the left Fig. , the resistivity of each layer of the model is
145 staggered along the fault, as shown in the in Fig. 1(b). The strata on the hanging wall of the fault move downwards,
146 which is a common normal fault. The model design mainly highlights the low-resistance target properties of the
147 broken and water-bearing fault zone, placing the fault zone in the layered, high-resistance surrounding rock.

148 **Model assumptions for CSAMT Response**

149 Based on the established simplified resistivity model of the geothermal system, the abnormal response of
150 CSAMT apparent resistivity in the model with different fault resistivity values, inclination angles and widths was
151 numerically simulated and analyzed. Since the emission source length and emission current are normalized during
152 the calculation of apparent resistivity, the emission source length and emission current are no longer listed. In
153 addition, in order to simulate the measured data as much as possible, Gaussian noise with a mean value of 3% of the
154 response amplitude is added to the response obtained by the numerical simulation. In order to compare with the
155 subsequent transient electromagnetic simulation more intuitively, noise is added to the electromagnetic field
156 response obtained by the numerical simulation, and then the apparent resistivity is further calculated. Following are
157 the parameters upon which our modeling is based on.

158 **A) CSAMT Response to the faults with different resistivities**

159 In the simplified resistivity model of the geothermal system established, the resistivity of the fault is $10\Omega\cdot\text{m}$.
160 usually in the stratum half-space, a fault can be regarded as an angularly inclined plate-like body extending
161 downward from the ground. There are a large number of cracks in the fault zone, which are filled by particles such as
162 breccia, and the resistivity of the filling is different, which determines Characteristics of fault resistivity. Therefore,

163 the resistivity of the fault is generally within a large range. We establish fault models with different resistivity values
164 (fault dip angle 30° , width 70m, and fault resistivity values 10, 50, $100\Omega\cdot\text{m}$), and perform forward simulation to
165 obtain each response, then calculate its resistivity. All responses are shown in the Fig. 2 (a-c).

166 **B) CSAMT Response to the faults with different dip angles**

167 The dip of the fault is usually an important indicator of detection. Based on this, we establish fault models with
168 different dip angles (fault resistivity value is $10\Omega\cdot\text{m}$, width is 70m, dip angles are 30° , 45° , 60°) and forward
169 modeling is performed, as shown in the Fig. 3(a-c).

170 **Model assumptions for TEM Response**

171 It is discussed above that, based on the numerical calculation of low-blocking layer models with different
172 resistivities and inclination angles; the ability of CSAMT to identify low-blocking layers was analyzed. As a
173 comparison, this section will carry out a numerical simulation analysis on the ability of the TEM method to identify
174 low-blocking layers. Similarly, starting from the resistivity and inclination of the fault, analyze its influence on the
175 TEM response. Because the apparent resistivity of the TEM method is divided into early and late stages, it is difficult
176 to obtain a stable apparent resistivity calculation formula covering all time channels. Therefore, the TEM analysis is
177 carried out for the derivative of the vertical magnetic field with respect to time (dB/dt).

178 The basic parameters of TEM numerical calculation are: the emission source is a 200m long single-turn square
179 loop, the derivative of the vertical magnetic field with respect to time is received at the center of the loop, the
180 emission waveform is a bipolar rectangular pulse, and the time range is 0.48ms-28.7ms, the number of time channels
181 is 21, and the distance of the receiving point is 100m. The specific geoelectric model is the same as in the previous
182 section. Similarly, in the transient electromagnetic response obtained by the simulation, random noise with a mean
183 value of 3% of the response amplitude is added.

184 **A) TEM Response to the faults with different resistivities**

185 A simplified model of the geothermal system with the same fault angle of 30° , the same width of 70m, and
186 different resistivity values of $10\Omega\cdot\text{m}$, $50\Omega\cdot\text{m}$, and $100\Omega\cdot\text{m}$ was established, and the voltage response was calculated.
187 Due to the large buried depth of the fault, the anomaly of the response mainly appears in the late time channel of the
188 transient electromagnetic response, and the early channel response is not greatly affected, as shown in the Fig. 4
189 (a-c)

190 **B) TEM Response to the faults with different dip angles**

191 A simplified model of the geothermal system with the same fault width of 70m, the same resistivity value of
192 $10\Omega\cdot\text{m}$, and different fault inclination angles of 30° , 45° , and 60° was established, and the voltage response was
193 calculated, as shown in the following Fig. 5(a-c).

194 **Advantages of comprehensive geophysical methods**

195 In a certain survey area, there are great variability in geological conditions and interference conditions. The use
196 of a single geophysical method for exploration will inevitably be affected by factors such as topography, surface
197 construction difficulty, shielding layer, noise current, and effective exploration depth. Restrictions, there are certain
198 limitations.

199 In order to overcome the limitations of a single method, the comprehensive geophysical exploration method
200 with CSAMT as the main and TEM as the supplement is used to conduct geothermal resource exploration in the
201 igneous rock area. Several methods can complement each other in a targeted manner and achieve relatively ideal
202 results (Zhang L et al., 2012; Zhang Y et al., 2012; Wu L, 2016):

203 (1) CSAMT has a large exploration depth and insufficient resolution for shallow layers, while TEM exploration
204 depth is relatively small and has a good detection effect on shallow layers. Several methods are integrated After
205 exploration, it can have a relatively reliable detection effect on the shallow and deep parts (Huo J et al., 2011).

206 (2) CSAMT has stronger anti-interference ability than TEM, and comprehensive exploration is adopted in the
207 section with strong electromagnetic interference signal, which can improve the accuracy of data collection (Chen W
208 et al., 2013);

209 (3) CSAMT has higher requirements for signal transmission and data collection, while the data collection of
210 TEM is relatively simple. Comprehensive exploration in a complex construction environment can reduce the impact
211 caused by construction;

212 (4) CSAMT has obvious response to high-resistance bodies in deep basement formations, and can be used to
213 detect high-resistance geological bodies such as igneous rock intrusion, while TEM has a better detection effect on
214 low-resistance bodies such as water-conducting fault structures. The method can increase the exploration resolution
215 in the vertical direction, adopt comprehensive methods for exploration, and effectively detect both high-resistance
216 bodies and low-resistance bodies in the vertical direction.

217 **Field Experimental example**

218 **Field Area Overview**

219 In order to verify the effect of comprehensive geophysical methods on geothermal resources exploration in
220 igneous rock areas, a geothermal resource exploration with comprehensive geophysical methods was carried out in a
221 place in Huaiaren County, Shanxi Province, China.

222 This area is located in the uplift belt on the west side of the central part of the Sanggan River New Rift in the
223 Datong Basin. It straddles the Huaiaren Sag and the Huanghualiang Sag uplift from west to east. Martial, Lower
224 Ordovician, Carboniferous, Permian, and Cenozoic (Q+N) strata, with Archean granite and Late Tertiary basalt
225 intrusions locally, among which basalt and deep igneous rocks of the Wutai Group are underground, which formed a
226 good storage area for geothermal resources.

227 This area straddles two structural units, the Huairan Graben and the Huangliang Horst, which are secondary
228 structures of the New Rift of Sanggan River. A series of NE-strike fault structures develop in the area. The
229 development of fault structures provides a better connection channel for various underground aquifers complete area
230 map is shown in Fig. 6.

231 As shown in Fig. 7, four CSAMT survey lines are arranged in the exploration area.

232 In the CSAMT detection, the instrument used is the GDP32II multifunctional electrical method workstation.
233 The transmitting pole distance $AB=1500m$, the transmitting current is 14-16A, the transmission distance is 6km; the
234 receiving point distance of line 59 and 64 is 50m, the receiving point distance of line 10 and line 60 is 100m, and the
235 signal frequency range is 0.125- 8192Hz. In the TEM detection, the instrument used is also the GDP32II
236 multifunctional electrical method workstation, and the center loop device is used for measurement. The transmitting
237 wire frame is a 600m×600m single-turn loop, powered by a generator, the fundamental frequency of the transmitting
238 source is 16Hz, and the transmitting current is 15A; the distance between the measuring points is 50m. After the
239 CSAMT measurement is completed, a TEM measurement line is arranged near the 60 line where the CSAMT
240 resistivity is more obvious, which is used to more accurately delineate the low resistance fracture zone, and combined
241 with the CSAMT and TEM results.

242 **Geophysical characteristics of Field Area**

243 Different rock formations have different conductivity. Generally speaking, in most igneous rock regions, due to
244 the ancient diagenesis age, after long-term metamorphism, the formation is compact and complete, and the fractures
245 are not developed. The resistivity is relatively uniform in the horizontal direction, and gradually increases with the
246 increase of the depth in the vertical direction, which is not conducive to Looking for geothermal resources (Li H,
247 2010).

248 In some igneous rock areas, the pore water of the overlying loose layer, after receiving the vertical infiltration
 249 replenishment of atmospheric precipitation and the intermittent leakage replenishment of surface water, can flow into
 250 the deep igneous rock and the fissures of the igneous rock basement through the fault fracture zone and rock fissures.
 251 Thermal storage aquifers form underground hot water and are stored in igneous rock formations. The resistivity of
 252 eruptive igneous rocks (such as basalt, rhyolite, etc.) is generally low ($20-500\Omega\cdot m$), which is lower than that of
 253 granite (greater than $500\Omega\cdot m$), but the resistivity of igneous rocks is generally greater than that of sediments
 254 Surrounding rock. Therefore, the difference in resistivity values between igneous rocks and sedimentary surrounding
 255 rocks can be measured by geophysical prospecting methods to determine the location of igneous rocks and igneous
 256 rocks, and then to search for geothermal resources (Zhang Q et al., 2016).

257 **Table 1.** Statistical table of different rock's resistivity in igneous area.

Rock Type	Resistivit	Rock Type	Resistivit
Sand	60-100	Conglomerat	50-200
Silty clay	14-25	Limestone	100-300
Basalt	20-500	Igneous rock	>1000
Granite	500-200		

258 On the other hand, in areas where faults are developed, the resistivity value will change. The activity of the fault may
 259 cause a fracture zone near the fault, and the fault will lead to the hydraulic connection between the upper and lower strata, thus
 260 forming a low-resistivity anomaly area near the fault that is close to the dip angle of the fault. Such low-resistance anomalies
 261 are in the resistivity. Generally, the cross-sectional view is relatively steep. By looking for such a steep anomaly with low
 262 resistivity, it can reflect the existence of faults, and then search for geothermal resources (Li W et al., 2002; Garyet G et al.,
 263 2006).

264 **Verified situation**

265 In the processing of the measured data, we first use the data preprocessing software of GDP32II to sort the collected data
266 and remove the dead pixels, and then use the CSAMT-2D software and TEM-1D software based on the OCCAM algorithm to
267 invert the data. The inversion results of CSAMT and TEM resistivity profiles are shown in Fig. 8(a-c).

268 **Discussions**

269 The results show that the influence of the fault on the CSAMT response is mainly in the low frequency range, and the
270 influence on the TEM response is mainly in the late stage. Because CSAMT low frequency band can still obtain high
271 signal-to-noise ratio data, and the signal-to-noise ratio of the late TEM response is generally lower, so CSAMT has a stronger
272 ability to distinguish low-blocking layers at this depth than TEM, and CSAMT can also distinguish faults. Upper and lower
273 plate. On the other hand, the TEM response can clearly distinguish the abnormal response caused by the width of the fault, but
274 the CSAMT response cannot be distinguished, which shows that the TEM has a stronger ability to describe the details of the
275 target body in the fault with low resistivity than the CSAMT; In addition, the faults are mainly manifested as obvious
276 resistivity dislocations on the apparent resistivity section of CSAMT, and the resistivity characteristics of the fault fracture
277 zone cannot be directly judged through the apparent resistivity section.

278 Although both methods can identify the low-blocking layer of the model, the two methods show obvious
279 complementarity in the detection depth and detail description ability, and are suitable for comprehensive application in the
280 detection of geothermal resources.

281 In general, the morphology of the resistivity profile of CSAMT and TEM is basically the same, and both show that the
282 resistivity is medium-low resistance in the medium and shallow layers, and the resistivity gradually increases as the depth
283 increases, and the deep substrate shows high resistance.

284 Comparing the detection effects of CSAMT and TEM, the differences are:

285 (1) TEM is better than CSAMT in the detection effect at shallow depths on the surface. CSAMT is affected by topography,
286 the low-resistance shielding interference of the Quaternary muddy sand and clay layer is relatively large, which shows
287 abnormal medium resistance, and the resistivity curve presents characteristics such as distortion, which reduces the resolution
288 of shallow layers to a certain extent. Although there is a blind zone with a depth of about 100m in TEM, the low-resistance
289 shielding layer at the shallow surface is less interference, and the resistivity value shows obvious regularity at the shallow
290 surface, which is consistent with the actual geological characteristics.

291 (2) CSAMT is better than TEM in the detection effect at large depths. In the 4500-10000 point section, CSAMT has
292 better data stratification in the deep part, while the TEM resistivity curve in this section is slightly confused, and the TEM
293 shows a circle of the resistivity curve in the 9000-9500 point section. Closed high-resistance abnormal value. This
294 high-resistance abnormal value should be a false abnormality caused by interference. The secondary field potential of the late
295 TEM measurement track also fluctuates greatly in this section, lacking regularity, indicating that CSAMT has better
296 anti-interference ability TEM.

297 (3) TEM and CSAMT have their own advantages in the detection of water-conducting fault structures.

298 Since the pure TE field mode of TEM is especially sensitive to low-resistance targets (Xue et al. 2013), this is more
299 obvious in the reflection of F1 fault. CSAMT hardly reflects the F1 fault in the low-resistance area in the shallow part, but there
300 is obvious low-resistance anomaly on the TEM profile. It can also be seen from the TEM secondary field potential
301 multi-channel map that there is an obvious abnormal high value of the secondary field potential in this area.

302 The advantage of CSAMT for fault detection is mainly reflected in the detection of deep high-resistance basement
303 interruption layer. In the sections of 5000m-5700m and 9500m-10000m, it is inferred that the buried depth of the Quaternary
304 and Tertiary loose deposits is about 500m. The lower part is the basement of igneous rock, and the resistivity reflects the
305 characteristics of high resistance. In the CSAMT cross-section map, these two sections appear as steep gradient zones, which
306 are inferred to be F2 and F3 faults, which can more intuitively distinguish the upper and lower walls of the fault.

307 (4) CSAMT is better than TEM for the detection effect of igneous rock basement. In the 5800m-9300m section, CSAMT
308 has a very obvious high-resistance response to the igneous rock basement, while the high-resistance response of TEM is not
309 obvious at this position, and it does not highlight the igneous rock basement.

310 After the completion of the geophysical prospecting construction, the drilling verification was carried out at 3350 point.
311 The borehole encountered underground hot water at 1610m; then a pumping test was carried out. According to the results of
312 the pumping test, the unit output of underground hot water in this area was 233m³/d. The water temperature is 58°C. This
313 result confirmed the occurrence of geothermal water in faults and igneous rock formations of the Wutai Group.

314 **Conclusion**

315 By numerical simulation, comparing the anomalies produced by the two methods on fault targets with different
316 resistivities and dips, it shows that the two methods have differences in their ability to identify and describe the details of
317 targets at different depths. Resolution of CSAMT for deep targets is stronger than TEM, and ability of TEM to describe the
318 details of shallow targets and faults is stronger than CSAMT. Both methods are capable of identifying targets at different
319 depths. However, in terms of depth of detection and ability to describe details, the two methods are obviously
320 complementary, and they are suitable for comprehensive application in the detection of geothermal resources. Moreover
321 actual detection results of CSAMT and TEM on the same survey line show that CSAMT is better than TEM in deep detection
322 and magmatic rock basement detection, while TEM is better than CSAMT in shallow detection and water-conducting fault
323 structure detection. The two methods of comprehensive survey overcome the limitations of a single method and have the effect
324 of complementing each other and confirming each other. In the exploration of geothermal resources in Yunzhong Town,
325 Huaiaren County, Shuozhou City, Shanxi Province, the following geological results were obtained: It is inferred that there are
326 three faults F1, F2, and F3, and the fault layer F1 is the main conduction channel for underground hot water; The deep basalt
327 basement or the mid-deep metamorphic rock basement of the Wutai Group is more likely to be a geothermal resource storage

328 structure. This study verifies the respective advantages and disadvantages of CSAMT and TEM in geothermal resource
329 detection.

330 **Declarations**

331 **Funding**

332 This Research is sponsored by the Project of National Natural Science Foundation of China (41674075), co-funded by
333 Guangxi Natural Science Foundation Innovative Research Team Project (2016GXNSFGA380004), and partially supported
334 by the project Research on Shear Resistance and Water Resistance Performance and Law of Bottom Water-Resistant Layer
335 of Karst Aluminum Mine Discharge Reservoir with grant number (42062015).

336 **Author contributions**

337 Yang Yang: Conceptualization, writing original draft preparation;

338 Bin Xiong: Methodology and supervision;

339 Sanxi Peng: Soft-ware, investigation, visualization;

340 Ibrar Iqbal: Validation, data curation, software;

341 Tianyu Zhang: Validation;

342 All authors read and approved the final manuscript.

343 **Availability of data and material**

344 The data that support the findings of this study are available from the corresponding author upon
345 reasonable request.

346 **Competing interests**

347 The authors declare no competing financial interest.

348 **Acknowledgements**

349 We gratefully acknowledge the Editors and Reviewers for providing thoughtful and useful
350 suggestions.

351 **References**

- 352 Chen W, Xue Gu (2013) Application on coal-mine voids detection with multi-device TEM technology. Progress in Geophysics
353 28(5): 2709-2717(in Chinese with English abstract)
- 354 Coggon JH (1971). Electromagnetic and electrical modeling by the finite element method. Geophysics, 36(1), 132-155.
- 355 Di Q, Wang R, Shi K, Li Y (2008) Applications of CSAMT for deep geothermal exploration in high level ambient noises areas
356 in Beijing. Journal of Engineering Geology 15(Suppl.): 203-207 (in Chinese with English abstract)
- 357 Dieter K, Paterson NR, Grant FS, (1969). IP and resistivity type curves for three-dimensional bodies. Geophysics, 34(4),
358 615-632.
- 359 Garyet G, DeGroot JR (2006) Robust estimation of geomagnetic transfer functions. Geophys Astr.Soc 87: 173-194.
- 360 Günther T, Rücker C, Spitzer K (2006). Three-dimensional modelling and inversion of DC resistivity data incorporating
361 topography-II. Inversion. Geophysical Journal International, 166(2), 506-517.
- 362 Huo J, Wu X, Li N (2011) Study on the depth of resistivity profiling method . Geophysical and Geochemical Computing
363 Technology 33 (4): 418-423(in Chinese with English abstract)
- 364 Iqbal I, Bin X, Tian G, Wang H, Sanxi P, YangY, Hanwu S, (2021). Near Surface Velocity Estimation Using GPR Data:
365 Investigations by Numerical Simulation, and Experimental Approach with AVO Response. Remote Sensing, 13(14),
366 2814.
- 367 Kang F (2018) Using the integrated electrical method to detect geothermal resources in Taipingwei of Qiyang County Hunan
368 Province. Geology and Exploration 53(6): 1155-1163(in Chinese with English abstract)

369 Li H (2010) Progresses in the Research of Igneous Rocks. *Geology and Exploration* 47(2): 180-186 (in Chinese with English
370 abstract)

371 Li W, Liao Z (2002) The application of TEM to geothermal exploration in tengchong . *Geophysical and Geochemical*
372 *Exploration* 26(5): 368-371(in Chinese with English abstract)

373 Mufti IR (1976). Finite-difference resistivity modeling for arbitrarily shaped two-dimensional structures. *Geophysics*, 41(1),
374 62-78.

375 Munoz Gerard (2004) Exploring for geothermal resources with electromagnetic methods. *Surveys in geophysics* 35.1:
376 101-122

377 Muraoka H, Uchida T, Sasada M, Yagi M, Akaku K, Sasaki M, Tanaka S, (1998). Deep geothermal resources survey program:
378 igneous, metamorphic and hydrothermal processes in a well encountering 500 C at 3729 m depth, Kakkonda, Japan.
379 *Geothermics*, 27(5-6), 507-534.

380 Okabe M (1981). Boundary element method for the arbitrary inhomogeneities problem in electrical prospecting. *Geophysical*
381 *Prospecting*, 29(1), 39-59.

382 Shi B (2005) *Geothermal resources and its development, utilization and protection*. Beijing :Chemical Industry Press

383 Spichak, Viacheslav, Adele M (2009) Electromagnetic sounding of geothermal zones. *Journal of Applied Geophysics* 68.4:
384 459-478[20] Fridleifsson, G. O, & Elders, W. A. (2005). The Iceland Deep Drilling Project: a search for deep
385 unconventional geothermal resources. *Geothermics*, 34(3), 269-285.

386 Spitzer K. (1995). A 3-D finite-difference algorithm for DC resistivity modelling using conjugate gradient methods.
387 *Geophysical Journal International*, 123(3), 903-914.

388 Wang G, Zhang F, Liu Z (2000) An Analysis of Present Situation and Prospects of Geothermal Energy Development and
389 Utilization in the World. *ACTA Geoscientia SINICA* 21(2): 134-139 (in Chinese with English abstract)

390 Wang L, Gong Yu, Yang Ha, Luo Y, Wang P (2018) Research and application of RDI in detecting orebody by aeronautical
391 transient electromagnetic method. *Progress in Geophysics* 33(4): 1707-1712 (in Chinese with English abstract)

392 Wu L (2016) Key issues of geothermal resource exploitation and utilization in the depression area of northern Shandong
393 Province . *Geology and Exploration* 52(2): 300-306(in Chinese with English abstract)

394 Yang L (2017) On deployment of high- temperature deep geothermal wells in typical areas with hot dry rock potential in China.
395 *Geology and Exploration* 53(2): 355-360 (in Chinese with English abstract)

396 Yang Y, Liu J, Zhang W, Gao G, Li B, Zhang F (2009) Applying comprehensive geophysical prospecting method in
397 geothermal exploration in Tianjin area. *Global Geology* 28(3): 351-360(in Chinese with English abstract)

398 Yin M, An C, Jin Y (2007) The application of the integrated geophysical and geochemical methods to the geothermal
399 exploration in a certain area of Inner Mongolia. *Geophysical and Geochemical Exploration* 31(4): 313-316(in Chinese
400 with English abstract)

401 Zhang L, Lin L (2012) Application of CSAMT in geothermal exploration. *Mining technology* 04: 128-129+133 (in Chinese
402 with English abstract)

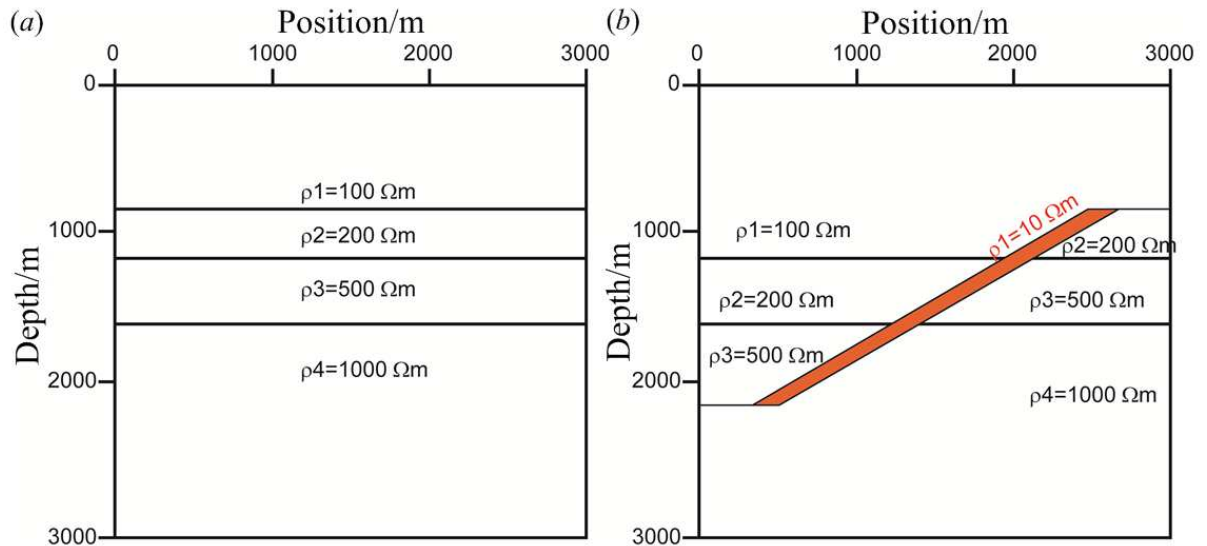
403 Zhang Q, Jin W, Wang J, Chen W, Li C, Jiao S, Shao Guol (2016) Relationship between magma-thermal field and hydrocarbon
404 accumulation. *Progress in Geophysics* 31(4): 1525-1541 (in Chinese with English abstract)

405 Zhang Y, Niu X, Han Z, Zhou J (2012) The application of Transient Electromagnetic Method in the work of mine flood
406 damage control. *Chinese Journal of Engineering Geophysics* 1.5: 418-423 (in Chinese with English abstract).

407 Zhao X, Zeng Z, Wu Z, Wang K, Li J, Xu T (2015) Delineating the area of HDR in Songliao basin using geophysical methods.
408 *Progress in Geophysics* 30(6): 2863-2869(in Chinese with English abstract).

409

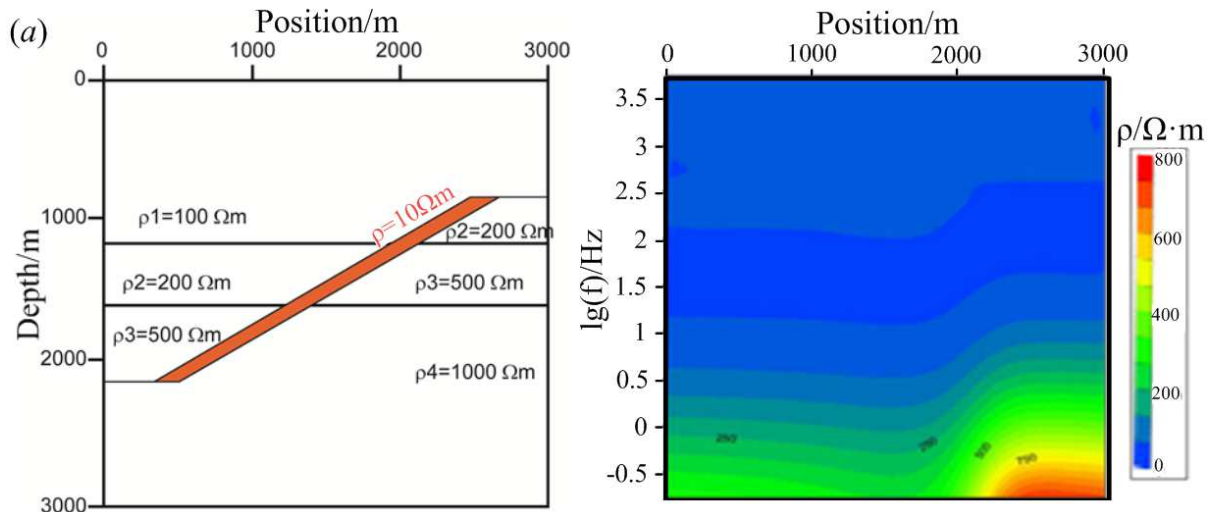
410



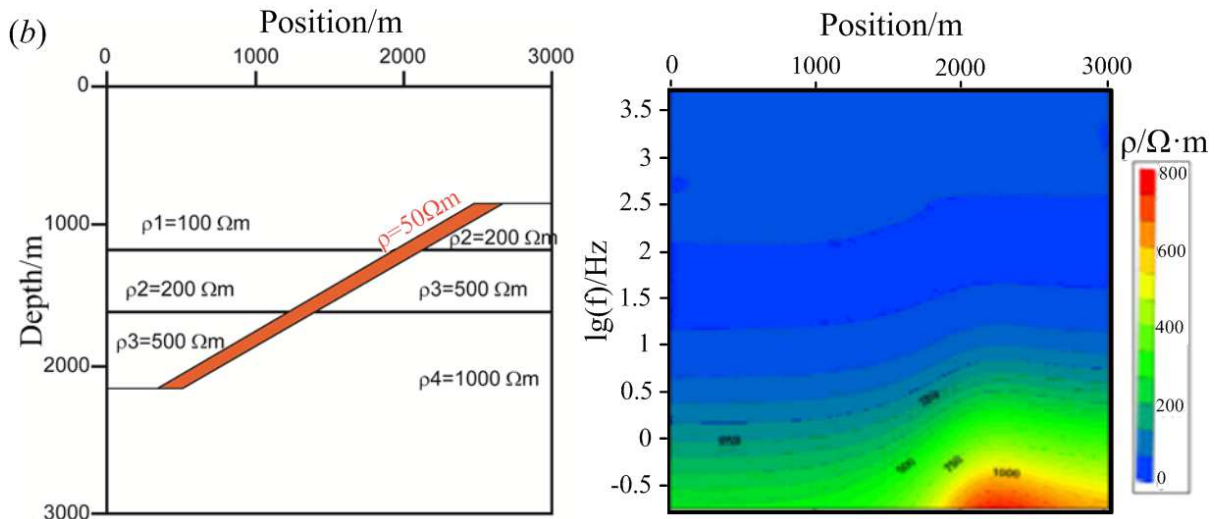
411

412 **Fig. 1** (a) Simplified resistivity model of geothermal system with fault as the target body. (b) The model on

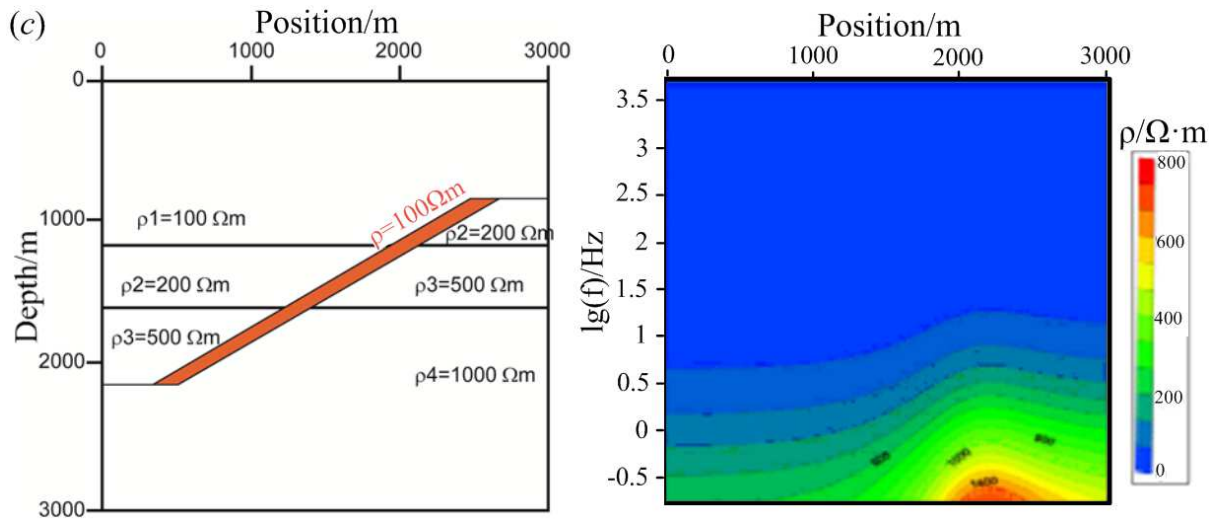
413 the left is the background model, and the model on the right is dislocated along the fault



414



415



416

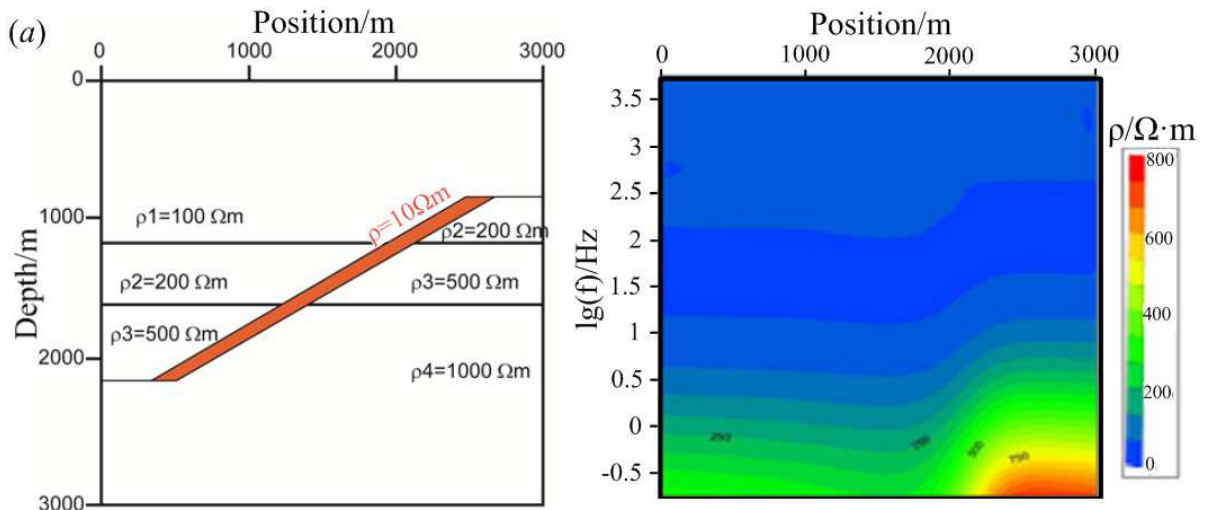
417 **Fig. 2** The model of fault resistivity is 10, 50, 100 $\Omega \cdot m$ and the cross-section view of resistivity Through the analysis of faults

418 with different resistivity values, it can be seen that when the fault resistivity is small (10, 50 $\Omega \cdot m$, less than the resistivity of the

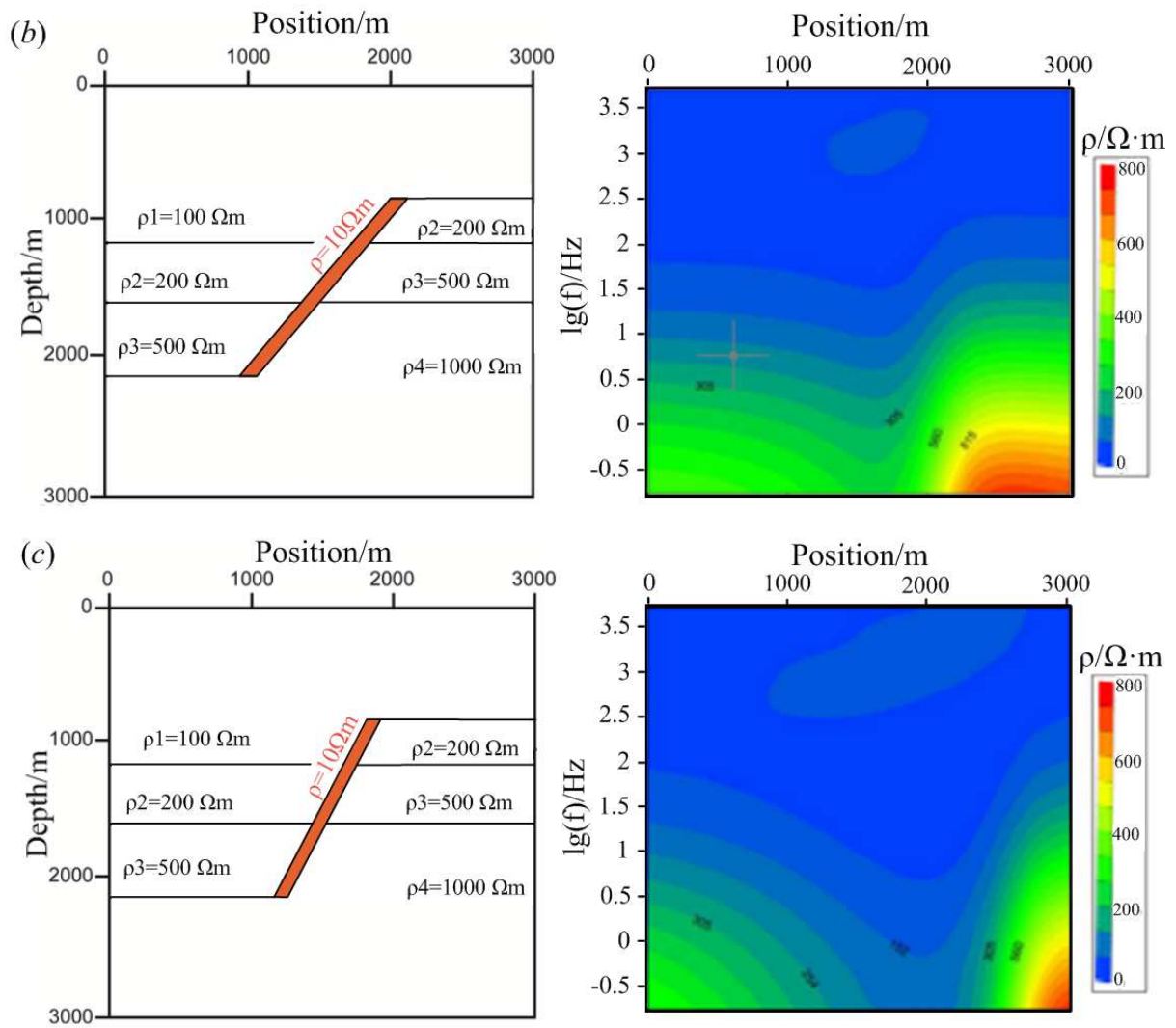
419 first layer of medium), the apparent resistivity curve near the fault is relatively smooth; As the fault resistivity increases, the

420 apparent resistivity curve rises more and appears to be significantly higher. Generally speaking, the difference in resistivity in

421 the fault zone can have obvious characteristics in the apparent resistivity profile.



422



423

424

425

Fig. 3 The model of fault dip angle is 30° , 45° , 60° and the cross-section view of resistivity from the above analysis, it can be

426

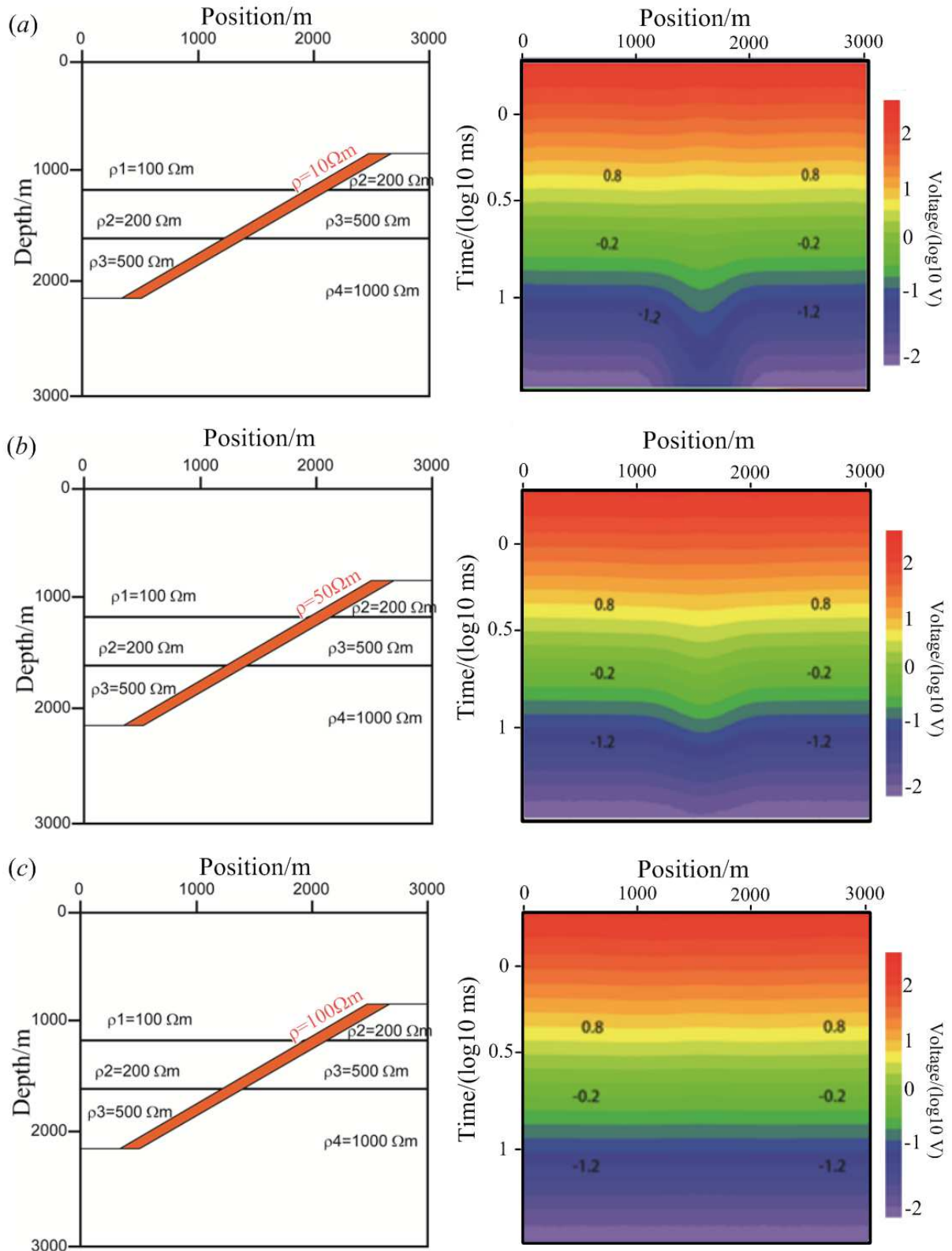
seen that when the dip angle of the fault is 30° , 45° , 60° , "sags" will appear in the interrupted layer of the apparent resistivity

427

profile; The greater the dip of the fault, the greater the degree of "sag" in the apparent resistivity profile; the dip reflected by the

428

apparent resistivity in the apparent resistivity profile is greater than the dip of the actual fault.



429

430

431

432

Fig. 4 The model of fault resistivity is 10, 50, 100 $\Omega\cdot\text{m}$ and the cross-section view of resistivity It can be seen from the above

433

analysis that when the resistivity of the fault zone is low, there is an obvious anomaly near the center of the fault, and the

434

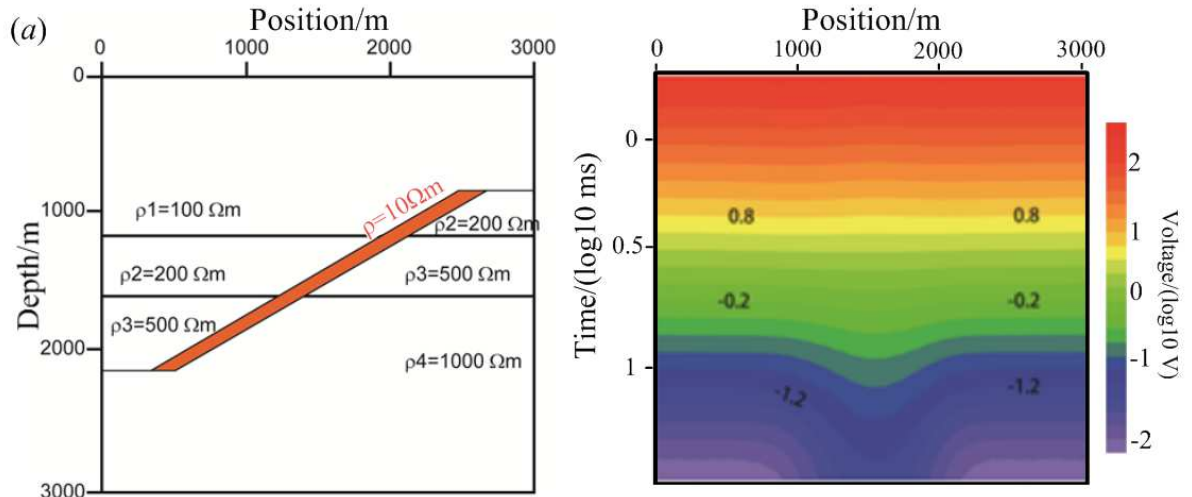
maximum value of the anomaly is located at the midpoint of the fault. The lower the resistivity, the more obvious the abnormal

435 response. When the resistivity of the fault zone is $100\Omega\cdot\text{m}$, the resistivity difference between it and the surrounding rock is

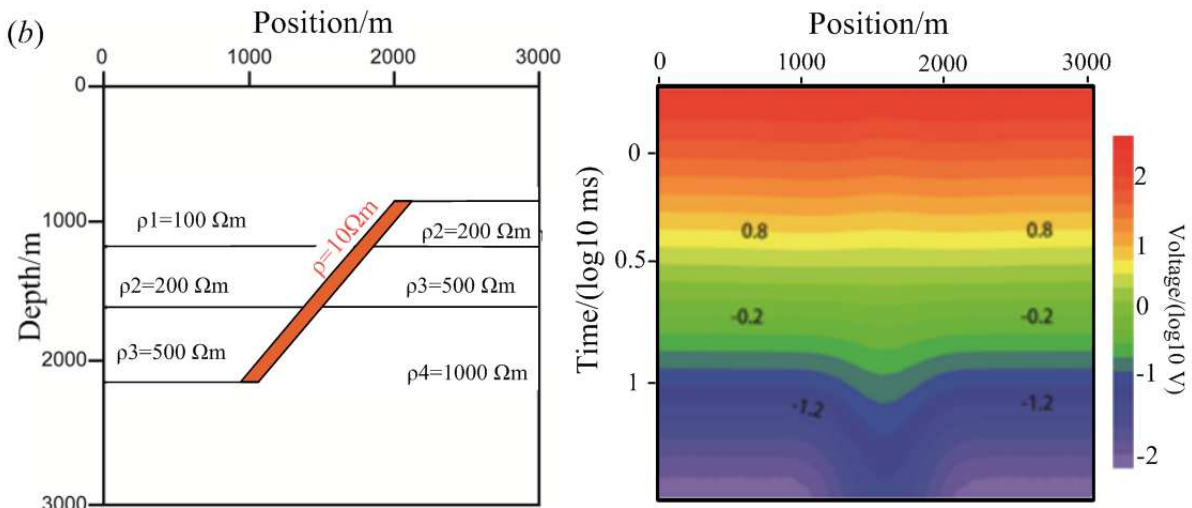
436 small, and no large anomaly can be generated on the resistivity profile. This shows that when the resistivity difference between

437 the fault and the surrounding rock is small, TEM is difficult to distinguish the existence of the fault.

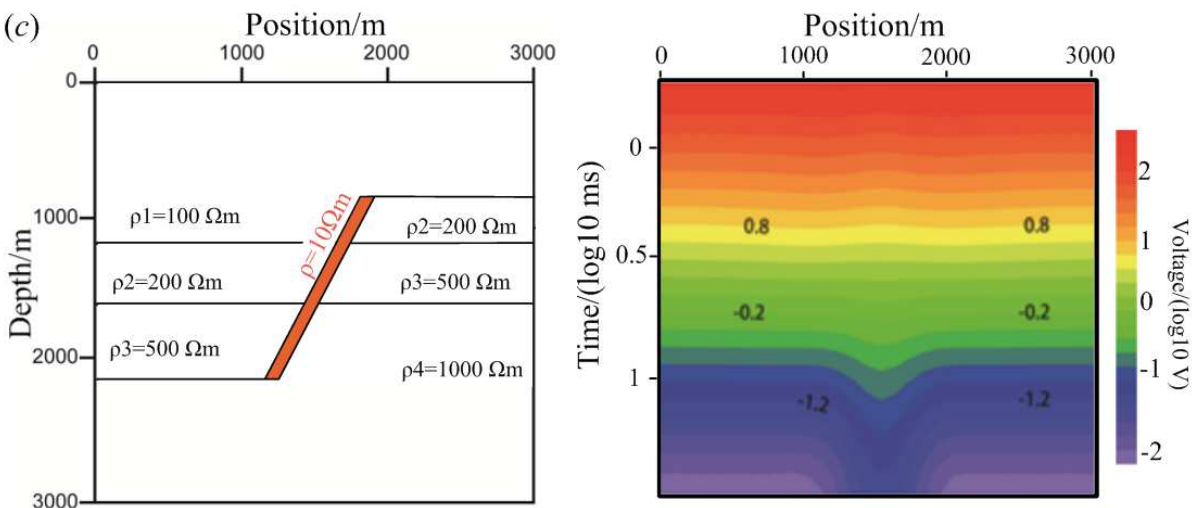
438



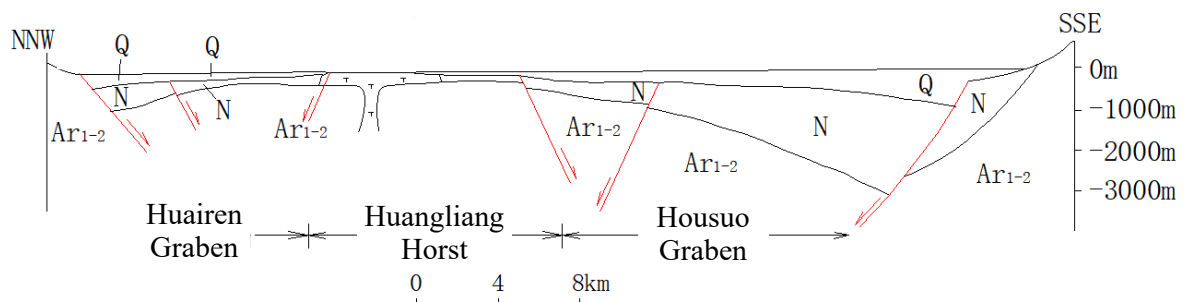
439



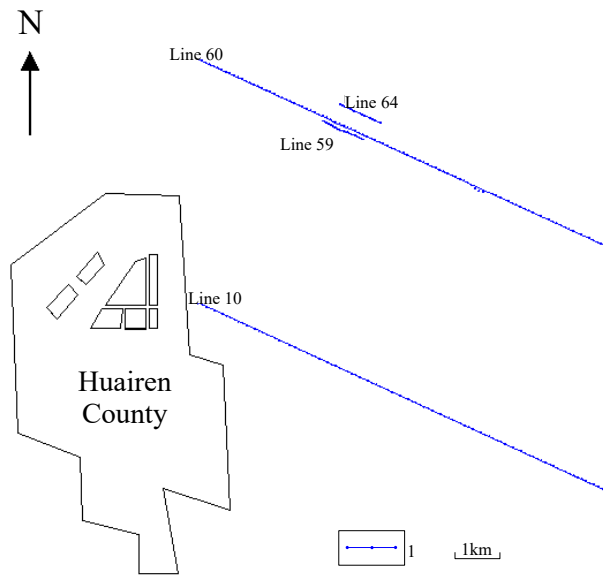
440



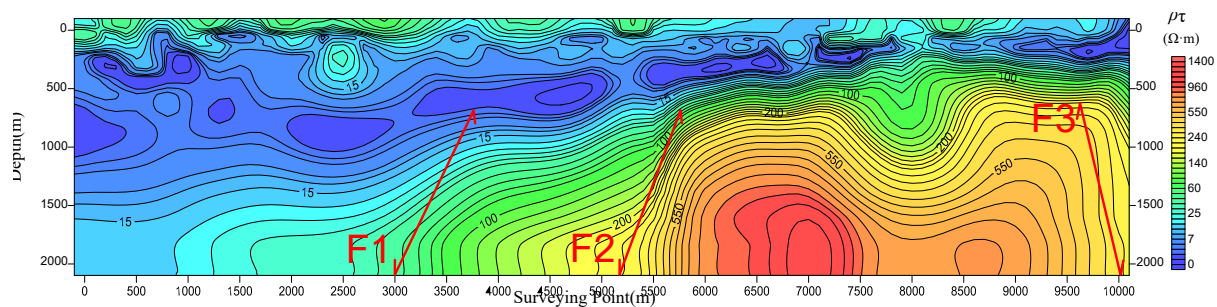
441 **Fig. 5** The model of fault dip angle is 30°, 45°, 60° and the cross-section view of resistivity through the above analysis, it can
 442 be seen that when the inclination of the fault with low resistivity in the geothermal system resistivity model is changed, the
 443 transient electromagnetic voltage response will change. With the increase of the dip angle of the fault, the width of the
 444 measuring point that can receive the abnormal response gradually decreases, and the amplitude of the abnormal response
 445 gradually increases, which shows that the transient electromagnetic exploration method is sensitive to the dip angle of the fault
 446 with low resistivity.



447
 448 **Fig.6** New rift of Sanggan River geologic section

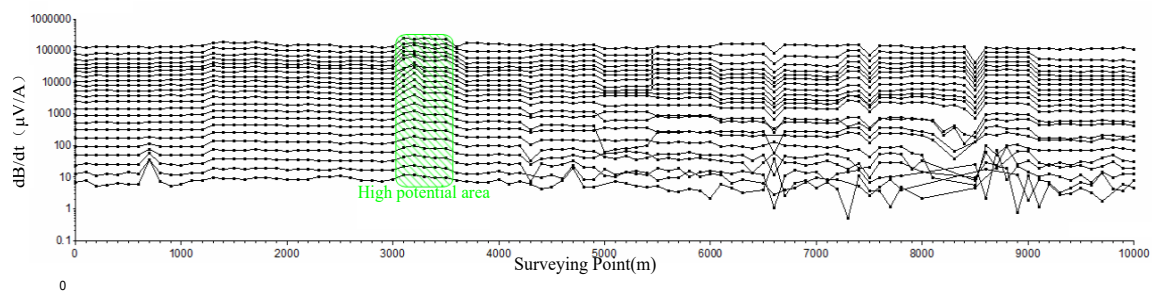


449
 450 **Fig. 7** Project layout (Surveying points and lines)



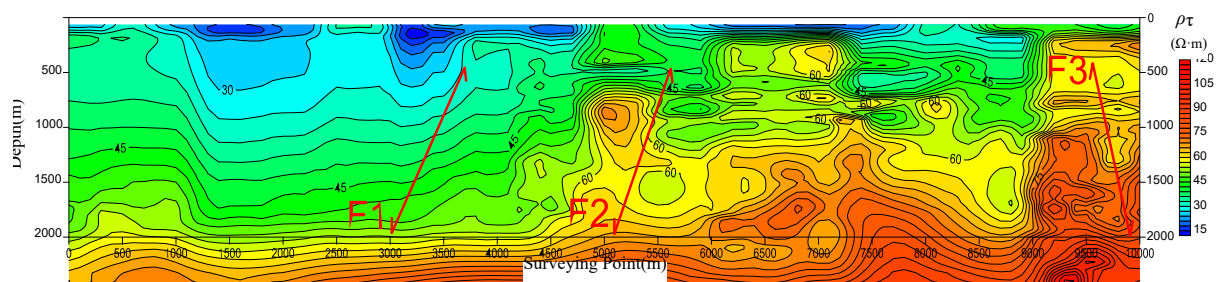
451

452 **Fig. 8 (a)** CSAMT resistivity profile of 60 Line



453

454 **Fig. 8 (b)** TEM secondary field profile of 60 Line



455

456 **Fig. 8(c)** TEM resistivity profile of 60 Line

457